


Waveguide-Mode-Enhanced Millimeter-Wave Photomodulators

I. R. Hooper^{✉*}

Department of Physics and Astronomy, University of Exeter, Stocker Road, Exeter EX4 4QL, United Kingdom

 (Received 4 December 2021; revised 26 January 2022; accepted 3 February 2022; published 1 March 2022)

The modulation of millimeter-wave transmission through a silicon wafer upon photoexcitation is typically very inefficient for off-the-shelf low effective charge carrier lifetime wafers, typically requiring tens of kilowatts of photoexciting intensity to generate significant modulation. Here we demonstrate that increasing the light-matter interaction for the millimeter waves using diffractively coupled waveguide modes leads to an increase in photomodulation efficiency of greater than two orders of magnitude, while maintaining the switching speed, of the order of $10 \mu\text{s}$, of the bare wafer.

DOI: [10.1103/PhysRevApplied.17.034001](https://doi.org/10.1103/PhysRevApplied.17.034001)

I. INTRODUCTION

The modulation of waves, whether spatial or temporal, is the basis of all photonic devices throughout the electromagnetic spectrum—from simple lenses and switches, to more complex spatial light modulators and signal-processing networks. In the optical region of the spectrum there are a wide range of available modulators including liquid crystal and micromirror-based devices, while at sub-gigahertz frequencies standard electronic components can be used [1]. However, in the millimeter-wave and terahertz spectral regions there is a lack of similarly mature technologies. Some possible candidates include electrical control of gated two-dimensional electron gases [2], including graphene [3], resonant metasurface elements [4–6], and LiNbO_3 [7]; thermal control of phase change materials such as VO_2 [8–11] and chalcogenide glasses [12,13]; and microelectromechanical-based systems [14–16].

While the above technologies show some promise, optical control of modulation is currently the most utilized method. This has been demonstrated in graphene [17], and in optically controlled diode-based systems at lower frequencies [18,19], but is more typically associated with changes in the conductivity of indirect bandgap semiconductors such as silicon and germanium via photoexcitation of free charge carriers [20–24]. Extensive reviews of the current state of the art in millimeter-wave and terahertz modulators can be found in [25–28].

The majority of the above references, regardless of the physical basis of the modulation, use resonant elements to enhance the light-matter interaction of the millimeter/terahertz wave with the modulating medium. These resonant elements are usually based on those seen

in so-called “metamaterials” or “metasurfaces” [29–32], where the material properties are determined by the resonant interactions with the structured elements, rather than by the material properties of the constituent parts. Often these resonant elements are based on variations of split-ring resonators [33]—essentially sub-wavelength metallic geometries with some degree of inductance and capacitance that support LC -type resonances. The millimeter/terahertz wave interacts with the resonant elements, generating enhanced fields within the modulating medium, resulting in a corresponding increase in modulation efficiency.

In some instances the modulating medium is itself structured to be the resonant element. For example, in [34] the VO_2 is structured so as to support Mie resonances, the enhanced fields of which are localized within the modulating medium. This can greatly enhance the light-matter interaction and thereby the modulation efficiency. We follow a similar approach here, but rather than structure the modulating medium, we use an external structure to couple into the resonant modes of a continuous slab of modulating medium. Specifically, we use a simple diffraction grating to couple energy into and out of the waveguide modes of a silicon wafer, which subsequently has its conductivity altered via a photoexciting optical beam. Since the fields associated with waveguide modes within a slab of material are localized within the medium, and since the coupling efficiency into these diffractively coupled waveguide modes (and hence the Q-factor and field enhancement) can be simply altered via the design of the diffraction grating, the light-matter interaction can be massively enhanced. This results in a smaller change in the conductivity of the wafer being needed to generate the same degree of modulation, and we demonstrate a greater than two orders of magnitude increase in photomodulator efficiency when compared to a bare silicon wafer.

*i.r.hooper@exeter.ac.uk

II. METHODS

Any dielectric slab bounded by dielectrics with lower refractive indices will support a family of bound waveguide modes [35]. The dispersion of these modes will depend upon the thickness and refractive index of the slab and the bounding media, and can be simply determined numerically. Here we use a silicon wafer of standard thickness $670\ \mu\text{m}$, which has a refractive index of $n = 3.42$. The dispersion relations of the transverse magnetic (TM) and transverse electric (TE) polarized waveguide modes supported by such a free-standing wafer are shown in Fig. 1, where k_{\parallel} is the in-plane wave-vector (parallel to the surface) and $k_g = 2\pi/\lambda_g$ is the grating vector resulting from a periodic perturbation with period $\lambda_g = 1.6\ \text{mm}$. Also shown are the scattered (diffracted) waveguide modes resulting from this periodic perturbation. For the wafer thickness of $670\ \mu\text{m}$ only the lowest-order TE and TM waveguide modes are supported within the frequency range of interest. The scattering due to the periodicity “folds” the waveguide modes back in reciprocal space such that they exist within the (unscattered) air light line, and can therefore be coupled to via incident plane waves. The period of $1.6\ \text{mm}$ was chosen so that the diffracted waveguide (DWG) modes would be excited at normal incidence at around $60\ \text{GHz}$, which is in the center of the V-band ($50\text{--}70\ \text{GHz}$) that will be used in experiments later in this paper.

Firstly, we characterized the 150-mm -diameter, $670\ \mu\text{m}$ -thick, float-zone intrinsic silicon wafer (resistivity

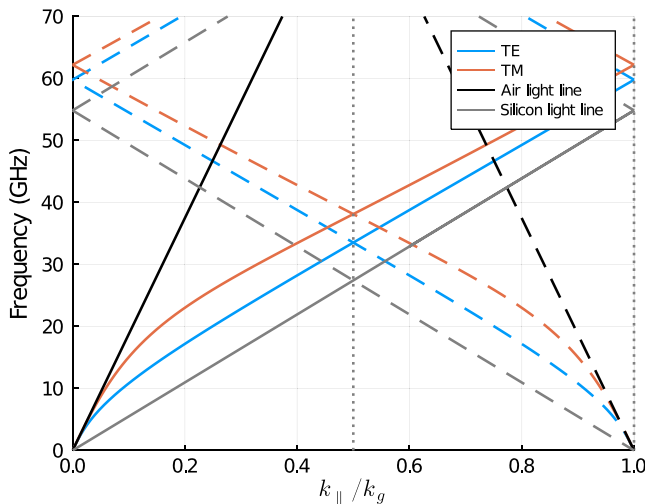


FIG. 1. Waveguide mode dispersions. The dispersion relations of the TE and TM waveguide modes supported by an intrinsic silicon wafer that is $670\ \mu\text{m}$ thick. Also shown as dashed lines are the corresponding scattered waveguide modes and light lines resulting from a periodic perturbation with a period of $1.6\ \text{mm}$. These scattered (diffracted) waveguide modes exist within the air light line and can thus be coupled to by incident plane wave radiation.

greater than $6000\ \Omega$) to be used in the DWG modulator. It is important that the wafer be undoped and have high resistivity so that any changes in the conductivity due to photoexcitation are maximized. The transmission of radiation in the range $50\text{--}70\ \text{GHz}$ through the wafer was measured at a 45° angle of incidence using standard gain horn antennas (Flann Microwave 25240 25 dB gain, with a half power beam width of approximately 10°) attached to an Anritsu Vectorstar MS4647B vector network analyzer (VNA), with the beam size at the wafer being approximately $100\ \text{mm}$. The wafer was subsequently photoexcited (flood illuminated) with $650\ \text{W/m}^2$ of $625\ \text{nm}$ light from a Thorlabs Solis 623C light-emitting diode (LED) source and DC2200 LED driver, and the transmission once again recorded. These were normalized to the signal with no sample in place, and are shown in Fig. 2(a). The peak in transmission at $67\ \text{GHz}$ corresponds to the Fabry-Pérot resonance supported within the thickness of the wafer. It is notable that the change in transmission upon photoexcitation resulting from the enhanced light-matter interaction afforded by the Fabry-Pérot resonance is significant, even though it has a relatively low Q-factor.

To characterize the switching speed of the modulation, one of the horn antennas was connected via a fast waveguide detector (Pasternack PE80T3002) to an oscilloscope (Siglent SDS2352X-E), and the continuous wave mode of the VNA was used to produce $67\ \text{GHz}$ radiation (on Fabry-Pérot resonance). The DC2200 LED driver was modulated with a period of $1\ \text{ms}$ and the transmitted intensity through the wafer upon switch-off of the photoexciting light was captured using the oscilloscope; see Fig. 2(b).

Also included in Fig. 2(b) is a fit from a COMSOL Multiphysics® [36] model using both the semiconductor and rf modules. The semiconductor module solves Poisson’s equation alongside the continuity equations for the charge carriers [37], allowing one to model the charge carrier distribution as a function of time throughout the wafer given some generation rate (in our case from photoexciting the wafer at one surface with light with energies above the band gap), and recombination rates both within the bulk and at the surfaces. The recombination rate within the bulk was determined by a Shockley-Read-Hall (SRH) model [38,39] with a long bulk lifetime of $10\ \text{ms}$ (note that this simply needs to be very long as the effective charge carrier lifetime is surface recombination limited [20]). Recombination at the surface was also modeled using an SRH model, but in this case the rate is determined by the surface recombination velocity (SRV). The mobilities of the electrons and holes, μ_e and μ_h , were specified as 1450 and $500\ \text{cm}^2\ \text{V}^{-1}\ \text{s}^{-1}$, respectively [40].

Initially, the steady-state charge carrier density distribution was calculated using a generation rate given by

$$G = \frac{Tk_a P_0 \lambda}{hc} \exp(-k_a x) \quad (1)$$

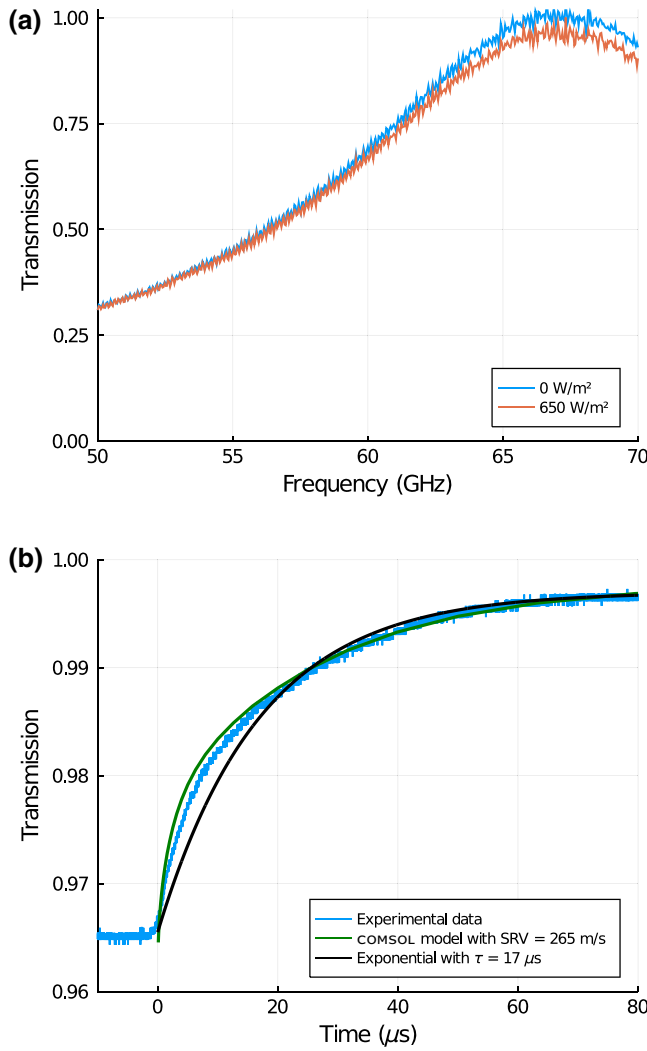


FIG. 2. Photomodulation of the bare silicon wafer. (a) The TE polarized millimeter-wave transmission through the 150 mm diameter, 670 μm thick, float-zone intrinsic silicon wafer (resistivity greater than 6000 ohms), used in the DWG modulator when unilluminated, and when photoexcited by 650 W/m^2 light from a Thorlabs Solis 623C LED source. The wafer was oriented at a 45° angle to both the millimeter-wave and optical beams. The peak in transmission at 67 GHz corresponds to the Fabry-Pérot resonance supported within the thickness of the wafer. (b) The time-dynamics upon switch-off of the photoexciting light source at 67 GHz. Also shown are fitted modeled data using a COMSOL Multiphysics model with the additional semiconductor and rf modules, and an exponential decrease in the change in ΔT with a time constant of $\tau = 17$ ms (see main text).

where $T = 0.651$ is the proportion of incident light transmitted into the wafer (as calculated using Fresnel's equations), $k_a = 4\pi n_i \lambda$ is the absorption coefficient with $n_i = 0.017$ being the imaginary part of the refractive index at a wavelength λ of 625 nm, $P_0 = 650 \text{ W}/\text{m}^2$ is the intensity of the light "incident" on the surface in order to mimic the photoexcitation used in the experiment, h and c are Planck's

constant and the speed of light *in vacuo* respectively, and x is the distance into the wafer. The time dynamics of the charge carrier distribution from this steady-state solution upon switching off the generation rate (turning off the photoexciting lamp) were subsequently calculated, giving the electron and hole densities, $N_e(x, t)$ and $N_h(x, t)$, as a function of position within the wafer at each time-step. These were subsequently used in a Drude model for both electrons and holes within the rf module to calculate the time-dependent spatial permittivity profile throughout the wafer, given by

$$\varepsilon_{\text{si}}(\omega, x, t) = \varepsilon_{\text{bg}} - \frac{\omega_{pe}(x, t)^2}{\omega(\omega + i\gamma_e)} - \frac{\omega_{ph}(x, t)^2}{\omega(\omega + i\gamma_h)} \quad (2)$$

where ω is the angular frequency of the radiation, $\varepsilon_{\text{bg}} = 11.7 + 0.003i$ is the background permittivity of the silicon due to the lattice, $\omega_{p(e,h)} = \sqrt{N_{e,h}(x, t)e^2 / (\varepsilon_0 m_{(e,h)})}$ are the plasma frequencies for the electrons and holes, with $m_e = 0.26m_0$ and $m_h = 0.38m_0$ being the conductivity effective masses [41]. $\gamma_{(e,h)} = e / (m_{(e,h)}\mu_{(e,h)})$, are the scattering rates of the electrons and holes, and e and ε_0 are the electron charge and permittivity of free space, respectively.

The transmission of TE polarized 67 GHz radiation incident at an angle of 45° through the wafer was calculated for each time-step used to calculate the time-varying permittivity profile of the silicon, as above, using COMSOL's rf module, thus mimicking the experimental setup. The rf module solves Maxwell's equations alongside the constitutive equations for a given geometry, material properties, sources, and so on, allowing the electromagnetic response of complex geometries to be calculated [42]. To obtain the model data presented in Fig. 2(b), "ports," which inject plane waves into and absorb plane waves from, the computational domain allowing calculation of reflection and transmission coefficients, were placed at the top and bottom of the geometry, while Bloch-Floquet periodic boundary conditions were placed at the sides of the unit cell that incorporated the silicon wafer free-standing in air. Thus the model represents an infinite plane wave incident upon an infinite wafer of silicon. A manual fitting procedure was undertaken, whereby the SRV of the surfaces was altered and the charge carrier dynamics and millimeter-wave transmission through the wafer as a function of time were calculated and compared to the experimental data. An SRV of 265 m s^{-1} was determined to result in the best fit. The reduction in ΔT as a function of time after switch-off is also expected to be approximately exponential, and Fig. 2(b) also includes such a curve with a time constant of 17 μs , indicating that this is the approximate switching speed of the modulation.

In our experiments described below, our diffraction grating was fabricated using standard printed circuit board

(PCB) techniques, and was placed adjacent to one of the surfaces of the silicon wafer. As such the 1.6 mm period used in the numerical calculations shown in Fig. 1 will not be correct since the boundary condition on that interface will have been altered by the presence of the PCB. We therefore underwent a design process using COMSOL Multiphysics in order to maximize the change in normal incidence TE polarized transmission upon photoexcitation for a DWG resonance around the center of our 50–70 GHz band. The PCB was modeled as 1.524-mm-thick Rogers RO4350B with 35- μm -thick copper. The design dielectric constant of Rogers R4350B was unknown in the frequency band of interest, but at 40 GHz it is 3.66 and as such this was used in the models. The thickness of the silicon wafer was 670 μm , and the charge carrier lifetime parameters determined by the previous wafer characterization were used to describe its response upon photoexcitation (i.e., a bulk lifetime of 10 ms and an SRV of 265 m/s for the surfaces). The steady-state charge carrier distribution for various photoexcitation intensities were calculated, and once again used within a Drude model within the rf module. The change in transmission through the DWG as a function of frequency upon photoexcitation could then be calculated for different periodicities and track widths of the copper diffraction grating using a modified version of the periodic model described previously (i.e., an infinite plane wave incident upon an infinite sample consisting of the wafer with the PCB diffraction grating adjacent to it). It was determined that a good candidate design had a period of 2.1 mm with copper track widths of 1.55 mm. A 150 mm square board was subsequently fabricated. A schematic of the final design is shown in Fig. 3.

To minimize any potential air gap between the PCB and silicon wafer, both were placed into a transparent polyethylene vacuum bag, which was then evacuated and sealed. This was subsequently mounted on a motorized rotation stage between the emitting and detecting horn antennas as described for Fig. 2(a), and the transmission through the modulator measured as a function of angle and frequency. In order to minimize interference effects between the horn antennas and the sample when close to normal incidence, thin layers of rf absorber were placed in front of each antenna. The measurements were then normalized to the spectra obtained with no sample in place.

III. RESULTS AND DISCUSSION

The polar angle (angle from the normal to the surface) and frequency-dependent transmission were measured for four different orientation–polarization combinations of the DWG modulator: TE and TM polarizations at 0 and 90° azimuthal angles (rotation of the grating around the normal to the surface; see Fig. 3 for a schematic of the polar and azimuthal angles). These were measured for no photoexcitation of the silicon and for illumination with the full

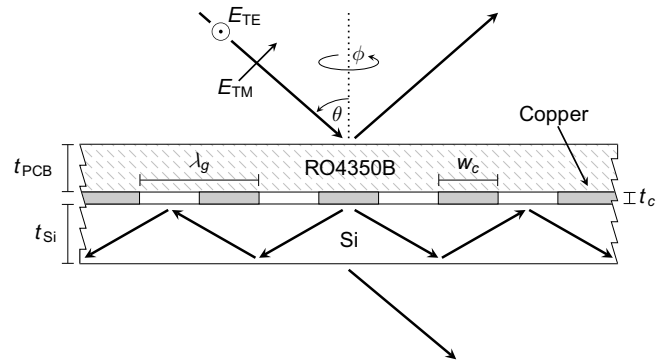


FIG. 3. DWG schematic. A one-dimensional diffraction grating consisting of parallel copper lines was etched into Rogers RO4350B printed circuit board and placed onto a silicon wafer. Also shown are the polar, θ , and azimuthal, ϕ , angles that determine the orientation of the modulator relative to the TE or TM polarized incident millimeter-wave radiation. Here, $\phi = 0^\circ$ corresponds to the grating vector being parallel to the plane of incidence (the orientation shown in the figure). The thickness of the PCB substrate, t_{sub} , copper tracks, t_c , and silicon wafer, t_{Si} , were 1.524 mm, 35 μm , and 670 μm , respectively. The period of the grating, λ_g , was 2.1 mm, and the track width, w_c , was 1.55 mm.

power of the Solis light source, which at the distance of the lamp from the sample was measured to be 650 W/m^2 . The results of these measurements, along with modeled data with no photoexcitation from our COMSOL Multiphysics model, are shown in Fig. 4.

The first column in Fig. 4 shows the predicted transmission through our modulator obtained from the COMSOL model for (a) TE polarization at 0° azimuth, (d) TM polarization at 0° azimuth, (g) TE polarization at 90° azimuth, and (j) TM polarization at 90° azimuth. We begin by using these results to understand the characteristics of the waveguide modes supported by our modulator, starting with Fig. 4(a). The band increasing in frequency as the angle reduces is the TE polarized scattered waveguide mode from the +1 grating vector. At normal incidence this interferes with the waveguide mode scattered from the -1 grating vector to create two standing wave modes, one with maxima at the center of the copper tracks and at the center of the gaps between them (this is the lower-energy mode), and the other with nodes that are 90° out of phase (the higher-energy mode). Due to their field symmetries only the lower-energy mode can be coupled to at normal incidence. Moving higher in frequency, the waveguide mode scattered from the -1 grating vector continues to increase in frequency with increasing angle before anticrossing with a waveguide mode supported within the PCB substrate (the character of these modes has been determined from field maps produced by the model).

The modes evident in Fig. 4(d) are similar to those in Fig. 4(a) except that these are TM polarized waveguide

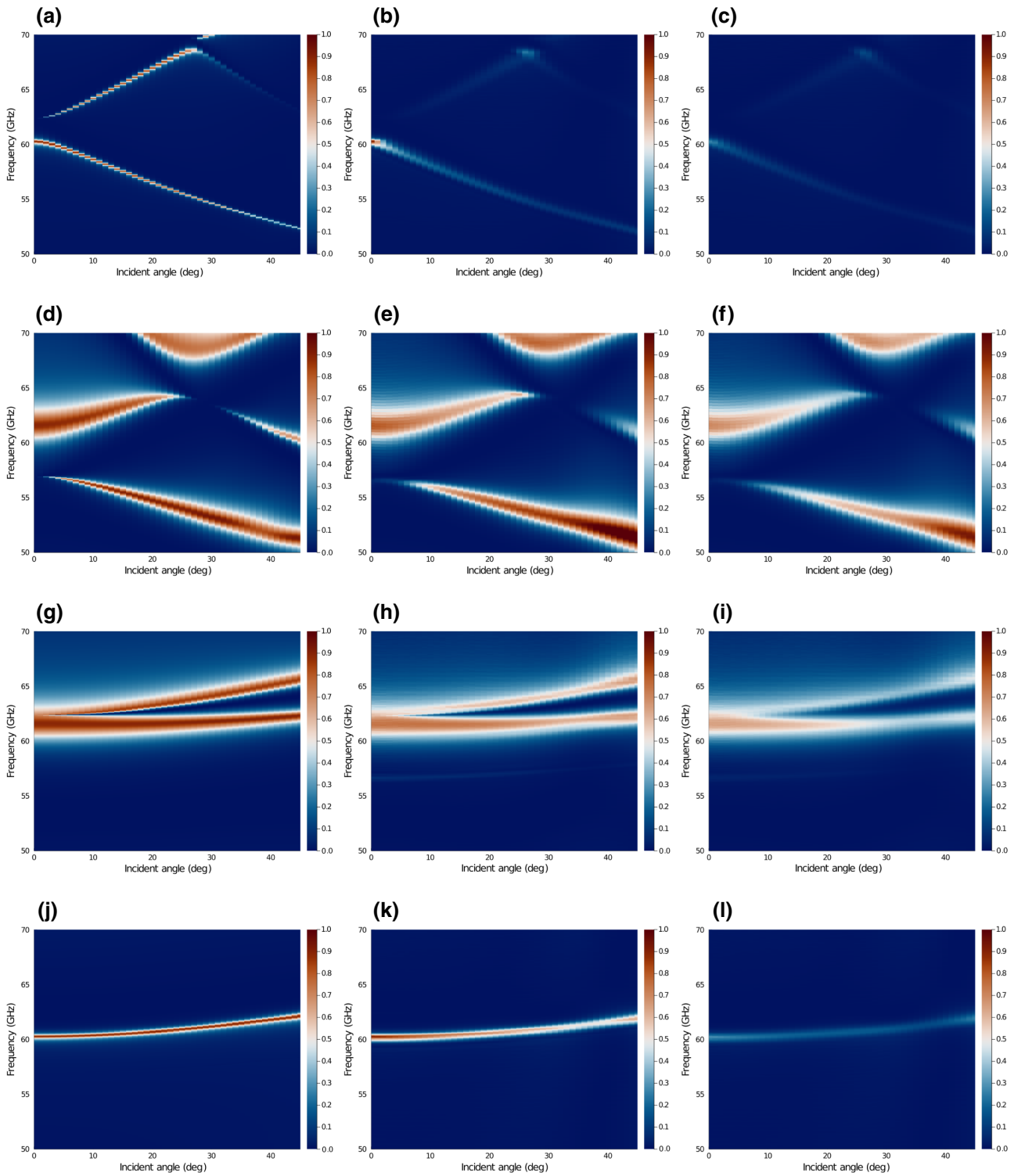


FIG. 4. Angle-dependent spectra. Transmission through the DWG modulator as a function of incident angle and frequency. The first column shows modeled results for the four cases: (a) TE polarized light at $\phi = 0^\circ$, (d) TM polarized light at $\phi = 0^\circ$, (g) TE polarized light at $\phi = 90^\circ$, (j) TM polarized light at $\phi = 90^\circ$. The second column shows experimental data for the same cases as the first column, while the third column shows equivalent experimental data when the silicon wafer was photoexcited by 650 W/m^2 light from a Thorlabs Solis 623C LED source.

modes. In this case, the Q-factors of the modes are significantly lower, and this is a result of the much higher diffraction efficiency from the grating when the E-field is perpendicular to the copper tracks (the diffraction efficiency at 60 GHz for the grating design into a half-space of silicon is approximately 0.1 when the E-field is perpendicular to the copper tracks, but just approximately 0.01 when parallel—from modeling). Since the diffraction efficiency into, and thus also out of, the waveguide mode is much greater when the E-field is perpendicular to the copper tracks, the radiative damping, and thus the width of the mode, will be correspondingly larger. Also notable is that it is the higher-energy mode that can be coupled to at normal incidence—with the reversal of the fields for TM polarization it is now the high-energy mode that has high H-field maxima at the center of the copper tracks and the gaps between them.

As we rotate the grating by 90° azimuthally [Figs. 4(g) and 4(j)], at normal incidence the response for TE polarization becomes that for TM polarization at a 0° azimuth (the E-field is now parallel to the copper tracks), and vice versa. We can understand the off-angle dispersion as a slice through the scattered waveguide dispersion in the (f, k_y) plane (here we define the x direction as parallel to the grating vector and the y direction as perpendicular to the grating vector and in the plane of the grating). The dispersion of the scattered waveguide mode in reciprocal space resembles a deformed cone centered at the grating vector (in the k_x direction). A slice through this cone in the (f, k_y) plane thus resembles a hyperbola—a standard conic section. The off-normal incidence splitting of the mode in the TE at 90° azimuth case is a result of an interaction with the higher-energy band edge of the mode seen at normal incidence in Fig. 4(a).

The nonphotoexcited experimental data (second column in Fig. 4) appears to compare well with the model data except in one case: there is a significant reduction in transmitted intensity when off normal incidence in the TE at 0° azimuth case [Fig. 4(b)]. This is a result of power being lost from the edges of the sample, and does not occur, or is a far smaller effect, in the other cases due to (i) the lower Q-factor of the resonances (the lifetimes of the modes are shorter, and hence they will propagate a shorter distance), and/or (ii) the modes are less dispersive (the group velocity is smaller, and energy is more likely to be scattered out of the waveguide mode before it encounters the edge of the sample).

When photoexcited with 650 W/m^2 (third column in Fig. 4) the transmitted intensity is reduced in all cases, but this reduction is far higher in the case where the electric field is parallel to the copper tracks. Since the Q-factor of the mode is much higher, the field strength within the wafer will also be correspondingly higher. Any absorption as a result of an increase in the imaginary part of the permittivity of the silicon upon photoexcitation will thus be

increased since absorption is proportional to $\epsilon_i E^2$. Indeed, the Q-factor of the modes at normal incidence in Figs. 4(b) and 4(k) is approximately 85 as compared to 12 for those in Figs. 4(e) and 4(h), and the corresponding modulation depths ($\Delta T/T_0$, where T_0 is the on-resonance transmission with no photoexcitation, and ΔT is the change in transmission upon photoexcitation) are 0.46 and 0.065. Note that the ratio of the Q-factors is almost the same as the ratio of the modulation depths (~ 0.7). We can also compare these values with those of the Fabry-Pérot resonance of

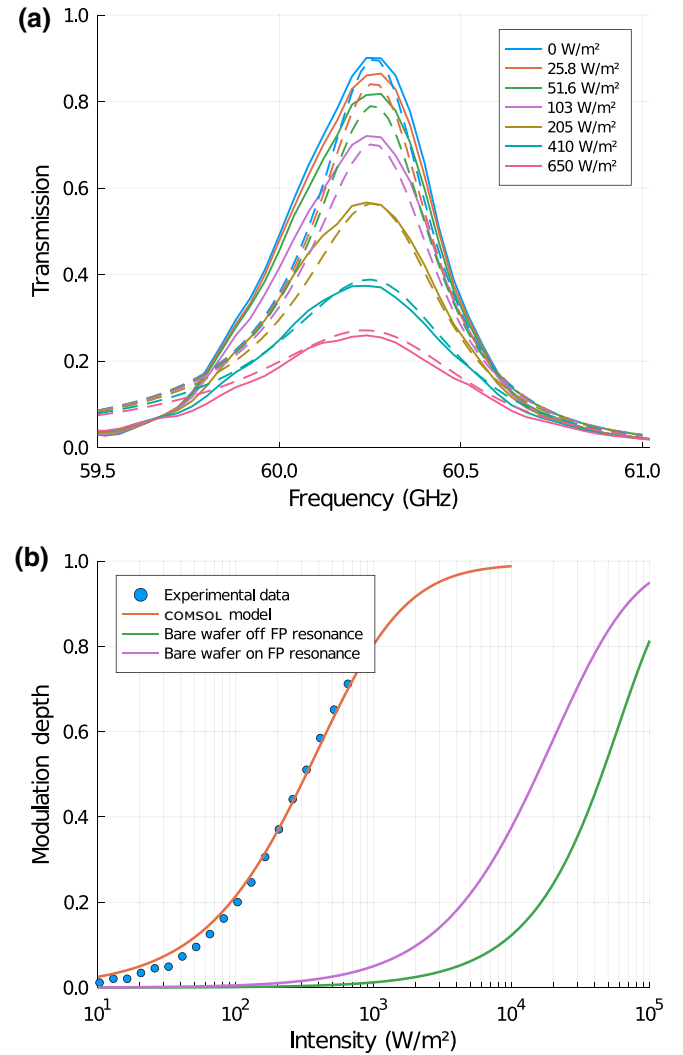


FIG. 5. Modulation efficiency. (a) The experimental (solid lines) and modeled (dashed lines) normal incidence TE polarized transmission through the DWG modulator when oriented at $\phi = 0^\circ$ for various photoexcitation intensities. (b) The modulation depth as a function of photoexcitation intensity. Also shown are results extracted from the COMSOL model of the DWG modulator and of the bare wafer both on (at 67 GHz) and off (at 50 GHz) the Fabry-Pérot resonance supported within its thickness [see Fig. 2(a)].

the bare wafer [Fig. 2(a)], which has a Q-factor of approximately 4.8 and a modulation depth, with the same optical illumination intensity, in the region of 0.025–0.035. The modulation depth and the Q-factor correlate closely once again, as would be expected.

The most efficient modulation occurs at normal incidence when the E-field is parallel to the copper tracks. To further investigate the modulation efficiency in this geometry we obtained transmission spectra for a range of optical illumination intensities, and a selection of these, again normalized to a measurement with no sample in place, along with comparisons to model data from COMSOL, is shown in Fig. 5(a). While the mode is somewhat broader in the experimental data, the change in transmission on resonance agrees well. In Fig. 5(b) we show the modulation depth on resonance as a function of illumination intensity for both the experimental data and the model. Also shown are the modeled modulation depths for the bare wafer on the Fabry-Pérot resonance (67 GHz), and off-resonance (50 GHz).

For the bare wafer, the enhanced light-matter interaction resulting from the Fabry-Pérot resonance increases the efficiency of photomodulation by approximately a factor of 3 (from approximately 45 kW/m^2 needed to achieve a modulation depth of 0.5, down to approximately 16 kW/m^2), while for our DWG modulator the efficiency is increased by a factor of approximately 150 (the intensity needed to achieve a modulation depth of 0.5 is further reduced to approximately 300 W/m^2).

Finally, in order to demonstrate that the switching speed of the DWG modulator remains the same as that of the bare wafer, the time dynamics after switching off the lamp were

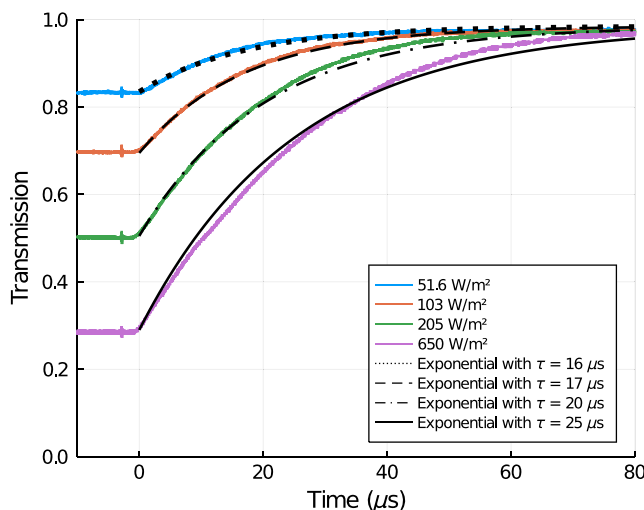


FIG. 6. Time dynamics of the DWG modulator. The normal incidence TE polarized transmission through the DWG modulator oriented at $\phi = 0^\circ$ as a function of time during switch-off for different photoexcitation intensities. Also shown are exponential curves with various time constants for comparison.

obtained for various photoexcitation intensities in the same way as for the bare wafer [Fig. 2(b)]. These are shown in Fig. 6, along with exponential change in transmission “fits.” The time constant of these fits increases slightly as the photoexciting intensity increases due to the change in transmission on-resonance as a function of the increase in the imaginary part of the permittivity of the wafer being nonlinear (this is also the reason for the form of the curves becoming less exponential in character). However, the time constants for small photomodulation depths are comparable to the $17 \mu\text{s}$ effective charge carrier lifetime that was measured for the bare wafer, confirming that the switching speed is determined solely by the effective charge carrier lifetime of the wafer, and that the increase in modulation efficiency arises only due to the increase in the light-matter interaction afforded by the excitation of the waveguide mode.

IV. CONCLUSIONS

By enhancing the light-matter interaction between a millimeter-wave beam and a silicon wafer using diffractively coupled waveguide modes, we have demonstrated a greater than two orders of magnitude increase in modulation efficiency of the transmission through the wafer upon photoexcitation of free charge carriers within the silicon. This increase in modulation efficiency is not at the cost of modulation speed, with the switching dynamics of the DWG-based modulator remaining unaltered.

While the use of waveguide modes to enhance photomodulation efficiency may be of limited utility due to the highly dispersive nature of the modes, it demonstrates the correlation between bandwidth and modulation efficiency in resonantly enhanced photomodulators. Alternative designs that support nondispersive narrow-band resonances could result in highly efficient modulators with applications in, for example, imaging systems and general purpose amplitude-based spatial light modulators for millimeter waves.

The research data supporting this publication are openly available from the University of Exeter’s institutional repository at Ref. [43].

ACKNOWLEDGMENTS

We thank Timothy Starkey for a critical reading of an earlier draft of this paper, and financial support from the EPSRC and QinetiQ Ltd via the TEAM-A Prosperity Partnership (Grant No. EP/R004781/1), and from the EPSRC via Grant No. EP/S036466/1: “Computational spectral imaging in the THz band.”

[1] D. M. Pozar, *Microwave Engineering* (Wiley, Hoboken, NJ, 2011), 4th ed.

- [2] T. Kleine-Ostmann, P. Dawson, K. Pierz, G. Hein, and M. Koch, Room-temperature operation of an electrically driven terahertz modulator, *Appl. Phys. Lett.* **84**, 3555 (2004).
- [3] B. Sensale-Rodriguez, R. Yan, M. M. Kelly, T. Fang, K. Tahy, W. S. Hwang, D. Jena, L. Liu, and H. G. Xing, Broadband graphene terahertz modulators enabled by intraband transitions, *Nat. Commun.* **3**, 780 (2012).
- [4] D. Shrekenhamer, S. Rout, A. C. Strikwerda, C. Bingham, R. D. Averitt, S. Sonkusale, and W. J. Padilla, High speed terahertz modulation from metamaterials with embedded high electron mobility transistors, *Opt. Express* **19**, 9968 (2011).
- [5] N. Karl, K. Reichel, H.-T. Chen, A. J. Taylor, I. Brener, A. Benz, J. L. Reno, R. Mendis, and D. M. Mittleman, An electrically driven terahertz metamaterial diffractive modulator with more than 20 db of dynamic range, *Appl. Phys. Lett.* **104**, 091115 (2014).
- [6] Z. Zhou, S. Wang, Y. Yu, Y. Chen, and L. Feng, High performance metamaterials-high electron mobility transistors integrated terahertz modulator, *Opt. Express* **25**, 17832 (2017).
- [7] J. Macario, P. Yao, S. Shi, A. Zablocki, C. Harrity, R. D. Martin, C. A. Schuetz, and D. W. Prather, Full spectrum millimeter-wave modulation, *Opt. Express* **20**, 23623 (2012).
- [8] T. Driscoll, H.-T. Kim, B.-G. Chae, B.-J. Kim, Y.-W. Lee, N. M. Jokerst, S. Palit, D. R. Smith, M. D. Ventra, and D. N. Basov, Memory metamaterials, *Science* **325**, 1518 (2009).
- [9] M. Liu, H. Y. Hwang, H. Tao, A. C. Strikwerda, K. Fan, G. R. Keiser, A. J. Sternbach, K. G. West, S. Kittiwatanakul, and J. Lu *et al.*, Terahertz-field-induced insulator-to-metal transition in vanadium dioxide metamaterial, *Nature* **487**, 345 (2012).
- [10] Y. Zhao, Y. Zhang, Q. Shi, S. Liang, W. Huang, W. Kou, and Z. Yang, Dynamic photoinduced controlling of the large phase shift of terahertz waves via vanadium dioxide coupling nanostructures, *ACS Photonics* **5**, 3040 (2018).
- [11] M. T. Nouman, J. Hwang, M. Faiyaz, G. Lee, D.-Y. Noh, and J.-H. Jang, Dynamic-metasurface-based cavity structures for enhanced absorption and phase modulation, *ACS Photonics* **6**, 374 (2019).
- [12] P. Pitchappa, A. Kumar, S. Prakash, H. Jani, T. Venkatesan, and R. Singh, Chalcogenide phase change material for active terahertz photonics, *Adv. Mater.* **31**, 1808157 (2019).
- [13] G. Linyang, M. Xiaohui, C. Zhaoqing, X. Chunlin, L. Jun, and Z. Ran, Tunable a temperature-dependent gst-based metamaterial absorber for switching and sensing applications, *J. Mater. Res. Technol.* **14**, 772 (2021).
- [14] Y. H. Fu, A. Q. Liu, W. M. Zhu, X. M. Zhang, D. P. Tsai, J. B. Zhang, T. Mei, J. F. Tao, H. C. Guo, X. H. Zhang, J. H. Teng, N. I. Zheludev, G. Q. Lo, and D. L. Kwong, A micro-machined reconfigurable metamaterial via reconfiguration of asymmetric split-ring resonators, *Adv. Funct. Mater.* **21**, 3589 (2011).
- [15] F. Ma, Y.-S. Lin, X. Zhang, and C. Lee, Tunable multiband terahertz metamaterials using a reconfigurable electric split-ring resonator array, *Light: Sci. Appl.* **3**, e171 (2014).
- [16] L. Cong, P. Pitchappa, C. Lee, and R. Singh, Active phase transition via loss engineering in a terahertz mems metamaterial, *Adv. Mater.* **29**, 1700733 (2017).
- [17] P. Weis, J. L. Garcia-Pomar, M. Höh, B. Reinhard, A. Brodyanski, and M. Rahm, Spectrally wide-band terahertz wave modulator based on optically tuned graphene, *ACS Nano* **6**, 9118 (2012).
- [18] I. V. Shadrivov, P. V. Kapitanova, S. I. Maslovski, and Y. S. Kivshar, Metamaterials Controlled with Light, *Phys. Rev. Lett.* **109**, 083902 (2012).
- [19] X. G. Zhang, W. X. Tang, W. X. Jiang, G. D. Bai, J. Tang, L. Bai, C.-W. Qiu, and T. J. Cui, Light-controllable digital coding metasurfaces, *Adv. Sci.* **5**, 1801028 (2018).
- [20] I. R. Hooper, N. E. Grant, L. E. Barr, S. M. Hornett, J. D. Murphy, and E. Hendry, High efficiency photomodulators for millimeter wave and thz radiation, *Sci. Rep.* **9**, 18304 (2019).
- [21] L. Cong, Y. K. Srivastava, H. Zhang, X. Zhang, J. Han, and R. Singh, All-optical active thz metasurfaces for ultra-fast polarization switching and dynamic beam splitting, *Light: Sci. Appl.* **7**, 28 (2018).
- [22] T. Matsui, R. Takagi, K. Takano, and M. Hangyo, Mechanism of optical terahertz-transmission modulation in an organic/inorganic semiconductor interface and its application to active metamaterials, *Opt. Lett.* **38**, 4632 (2013).
- [23] S. Augustin, J. Hieronymus, P. Jung, and H.-W. Hübers, Compressed sensing in a fully non-mechanical 350 ghz imaging setting, *J. Infrared, Millimeter, Terahertz Waves* **36**, 496 (2015).
- [24] M. Kafesaki, N. H. Shen, S. Tzortzakis, and C. M. Soukoulis, Optically switchable and tunable terahertz metamaterials through photoconductivity, *J. Opt.* **14**, 114008 (2012).
- [25] Z. T. Ma, Z. X. Geng, Z. Y. Fan, J. Liu, and H. D. Chen, Modulators for terahertz communication: The current state of the art, *Research* **2019**, 6482975 (2019).
- [26] M. Rahm, J.-S. Li, and W. J. Padilla, THz wave modulators: A brief review on different modulation techniques, *J. Infrared, Millimeter, Terahertz Waves* **34**, 1 (2013).
- [27] L. Wang, Y. Zhang, X. Guo, T. Chen, H. Liang, X. Hao, X. Hou, W. Kou, Y. Zhao, T. Zhou, S. Liang, and Z. Yang, A review of thz modulators with dynamic tunable metasurfaces, *Nanomaterials* **9**, 965 (2019).
- [28] Q. He, S. Sun, and L. Zhou, Tunable/reconfigurable metasurfaces: Physics and applications, *Research* **2019**, 1849272 (2019).
- [29] N. Meinzer, W. L. Barnes, and I. R. Hooper, Plasmonic meta-atoms and metasurfaces, *Nat. Photonics* **8**, 889 (2014).
- [30] H.-T. Chen, A. J. Taylor, and N. Yu, A review of metasurfaces: Physics and applications, *Rep. Prog. Phys.* **79**, 076401 (2016).
- [31] W. T. Chen, A. Y. Zhu, and F. Capasso, Flat optics with dispersion-engineered metasurfaces, *Nat. Rev. Mater.* **5**, 604 (2020).
- [32] J. Hu, S. Bandyopadhyay, Y.-h. Liu, and L.-y. Shao, A review on metasurface: From principle to smart metadevices, *Front. Phys.* **8**, 586087 (2021).

- [33] J. Pendry, A. Holden, D. Robbins, and W. Stewart, Magnetism from conductors and enhanced nonlinear phenomena, *IEEE Trans. Microw. Theory Tech.* **47**, 2075 (1999).
- [34] N. A. Butakov, I. Valmianski, T. Lewi, C. Urban, Z. Ren, A. A. Mikhailovsky, S. D. Wilson, I. K. Schuller, and J. A. Schuller, Switchable plasmonic-dielectric resonators with metal-insulator transitions, *ACS Photonics* **5**, 371 (2018).
- [35] P. v. Tien, Light waves in thin films and integrated optics, *Appl. Opt.* **10**, 2395 (1971).
- [36] COMSOL multiphysics® v. 6.0, COMSOL AB, Stockholm, Sweden (2021).
- [37] *Semiconductor Module User's Guide* (COMSOL AB, Stockholm, Sweden, 2021).
- [38] W. Shockley and W. T. Read, Statistics of the recombinations of holes and electrons, *Phys. Rev.* **87**, 835 (1952).
- [39] R. N. Hall, Electron-hole recombination in germanium, *Phys. Rev.* **87**, 387 (1952).
- [40] D. Klaassen, A unified mobility model for device simulation-I. model equations and concentration dependence, *Solid State Electron.* **35**, 953 (1992).
- [41] A. Kannegulla, M. I. B. Shams, L. Liu, and L.-J. Cheng, Photo-induced spatial modulation of THz waves: Opportunities and limitations, *Opt. Express* **23**, 32098 (2015).
- [42] *RF Module User's Guide* (COMSOL AB, Stockholm, Sweden, 2021).
- [43] <https://doi.org/10.24378/exe.3823>.